

Direct comparison of shadowgraphy and x-ray imaging for void fraction determination

Dash, Amitosh; Jahangir, Saad; Poelma, Christian

DOI

[10.1088/1361-6501/aaea49](https://doi.org/10.1088/1361-6501/aaea49)

Publication date

2018

Document Version

Final published version

Published in

Measurement Science and Technology

Citation (APA)

Dash, A., Jahangir, S., & Poelma, C. (2018). Direct comparison of shadowgraphy and x-ray imaging for void fraction determination. *Measurement Science and Technology*, 29(12), Article 125303. <https://doi.org/10.1088/1361-6501/aaea49>

Important note

To cite this publication, please use the final published version (if applicable). Please check the document version above.

Copyright

Other than for strictly personal use, it is not permitted to download, forward or distribute the text or part of it, without the consent of the author(s) and/or copyright holder(s), unless the work is under an open content license such as Creative Commons.

Takedown policy

Please contact us and provide details if you believe this document breaches copyrights. We will remove access to the work immediately and investigate your claim.

PAPER • OPEN ACCESS

Direct comparison of shadowgraphy and x-ray imaging for void fraction determination

To cite this article: Amitosh Dash *et al* 2018 *Meas. Sci. Technol.* **29** 125303

View the [article online](#) for updates and enhancements.

Direct comparison of shadowgraphy and x-ray imaging for void fraction determination

Amitosh Dash[✉], Saad Jahangir[✉] and Christian Poelma[✉]

Multiphase Systems (Process & Energy), Mechanical, Maritime and Materials Engineering, Delft University of Technology, Mekelweg 2, 2628 CD Delft, The Netherlands

E-mail: a.dash@tudelft.nl

Received 17 August 2018, revised 15 October 2018

Accepted for publication 22 October 2018

Published 16 November 2018



CrossMark

Abstract

A quantitative analysis of two imaging modalities, shadowgraphy and x-ray imaging, is presented in the framework of void fraction determination. The need for this arises from the fact that shadowgraphs are sometimes utilized to quantify void fraction profiles, which is an unproven method. Time-averaged x-ray images are used to evaluate the performance of the time-averaged shadowgraphs. The case of a cavitating flow through an axisymmetric converging-diverging nozzle ('venturi') is considered, for three separate cavitation numbers. The complex nature of the cavitating flow through the venturi manifests itself in the occurrence of three distinct regimes: a swarm of tiny bubbles; a large, coalesced cavity near the wall; and a drifting/collapsing cavity. The flow regime governs the performance of shadowgraphy for void fraction determination, with two of the three regimes deemed acceptable for shadowgraphy. The quantitative comparison exemplifies that sole reliance on shadowgraphy may lead one to draw improper conclusions on the void fraction distributions, even at a qualitative level.

Keywords: shadowgraphy, x-ray imaging, cavitation, venturi, void fraction estimation

(Some figures may appear in colour only in the online journal)

1. Introduction

There are many industrial applications involving multiphase flows, including sprays, fluidized beds, bubbly flows and cavitating flows. A common characteristic of these flows is that they are often optically opaque. This is due to multiple scattering of visible light by particles/bubbles in its path. More often than not, simple optical techniques are limited to analyzing phenomena occurring close to the wall region. Owing to the lack of penetrability of visible light in such optically opaque flows, alternative techniques have been developed to quantitatively characterize the phenomena occurring in the interior of the flow [1, 2]. X-ray computed tomography (CT) is an appropriate choice for an accurate analysis of the internal structure of the flow, as it is able to provide detailed information on the spatial distribution of void fractions [3, 4]. However, a major disadvantage of this technique is the high barrier to entry. Of the multiphase flows introduced earlier, cavitating flows are slightly different, as a predetermined global void fraction of a certain phase cannot be introduced into the flow. This is due

to the phenomenon of cavitation, where liquid vaporizes upon reaching a pressure below its vapor pressure. Void fraction is a major quantity of interest in cavitating flows as it can be used to demarcate the distinct shedding mechanisms [5, 6].

For certain regimes of multiphase flows, such as stratified flows or slug flows, void fractions can be determined by applying a simple pixel counting or greyscale intensity based technique onto shadowgraphy images. For instance, in some studies [7–9], a plane perpendicular to the flow direction (i.e. a cross-section of the pipe) was illuminated and imaged. The void fractions were then evaluated based on a pixel counting technique. Alternatively, the center-plane could be used. However, this would rely on an assumption about the three-dimensional (3D) structure of the flow (for example an axisymmetric structure of the slug). Such greyscale intensity based techniques may not always be appropriate to other regimes such as dispersed flows or annular flows. Nevertheless, various studies exist where the above pixel counting and/or greyscale intensity based techniques have been employed to determine void fractions, in flow regimes where it may not



be perfectly applicable [10–18]. In the above cases, the flow characteristics are often assumed to be two-dimensional (2D) or the void fractions are estimated from instantaneous images. This approach is understandable, due to the limited access to more advanced measurement facilities like x-ray CT.

Due to the continued usage of shadowgraphy for optically dense systems, even for void fraction estimation, questions persist over its applicability to such systems. The lack of applicability of shadowgraphy for cavitating flows has been qualitatively demonstrated by comparing images obtained by simple shadowgraphy/photography and CT [19–21]. Mitroglou *et al* [20] have reported a good qualitative correspondence between the vapor cloud *shapes* identified via time-averaged intensities of shadowgraphy images and line-integrated projections of 3D CT data. Lorenzi *et al* [21] too have compared time-averaged results obtained via the two imaging modalities and have concluded that planar shadowgraphy can create a false impression of the cavitation structures in the third dimension. These qualitative results [20, 21] already act as a deterrent for researchers aiming to extract void fractions through shadowgraphy like techniques. However, there has not been a *quantitative* comparison between images obtained by these two modalities (shadowgraphy and x-ray imaging), to the best of the authors' knowledge. A quantitative analysis could shed further light onto this matter.

The current study is thus concerned with a quantitative comparison between the time-averaged images of a 3D cavitating flow in an axisymmetric converging-diverging nozzle ('venturi'), recorded by two different imaging modalities: shadowgraphy and x-ray imaging. A venturi has been selected as a test case for the present study, owing to the complex nature of the flow through it. Thus, distinct flow regimes suitable for the current comparative analysis are present. The greyscale intensities in these images are a function of the void fractions occurring in the flow as well as the working mechanisms of the techniques. X-ray imaging, being the more reliable technique for void fraction estimation (owing to its penetrability in optically dense media), is then used to adjudge the fidelity of void fraction estimation (either qualitative or quantitative) via shadowgraphy in 3D cavitating flows. Regimes where (qualitative) void fraction estimation from shadowgraphy may still be applicable are also identified.

The remainder of the article is structured as follows: details of the experimental setups as well as the image processing steps to make images from the two modalities comparable are available in section 2. In section 3, a quantitative comparison between the greyscale intensities, obtained from the two measurement techniques is performed. The results are discussed in further depth in section 4, which includes the delimitation of regimes where shadowgraphy may still provide a legitimate interpretation of void fractions in 3D cavitating flows. Finally, the major findings of this study are summarized in section 5.

2. Methodology

Details of the experimental setups for both techniques, image acquisition and image processing are described in this section. The quality of the imaging techniques is also evaluated. This

is especially necessary for the x-ray images as they are later used as the yardstick while judging the shadowgraphs.

2.1. Setup

The schematic of the flow setup utilized for the experiments is illustrated in figure 1. The flow is driven by a centrifugal pump, while a combination of a water column and a vacuum pump is used to control the global static pressure of the flow loop. Further details are available in Jahangir *et al* [22]. The venturi, with a throat diameter (D_0) of 16.67 mm, is milled out from a rectangular block of polymethylmethacrylate (PMMA) and polished. This is done to minimize image distortion inside the venturi. A schematic of the venturi cross-section is shown in figure 1 (inset).

The intensity of cavitation is often described by the 'cavitation number' ($\sigma = \frac{p - p_v}{\frac{1}{2}\rho u_0^2}$). Here, p is the pressure at a reference position (the pressure recovery section in the current study), p_v is the vapor pressure of the fluid (calculated at the measured temperature), ρ is the density of the fluid, and u_0 is the reference velocity (the velocity at the venturi throat in the current study). In the current study, cavitation occurs only when the cavitation number is below unity. Moreover, the lower the cavitation number, the higher the cavitation intensity.

Shadowgraphs were recorded at 800 Hz for 4 s by a Photron Fastcam APX RS, in combination with a 105 mm/2.8 FX AF MICRO-NIKKOR object-glass. The CMOS sensor had a bit depth of 10. The camera was operated at a $f_\#$ of 2.8 with an exposure time of 111 μ s. Images with a resolution of 1024×336 pixels were recorded, resulting in a spatial resolution of approximately 0.15 mm. A LED panel was used for a uniform back-illumination. For the x-ray measurements, a source-detector pair was used to measure the attenuation of the x-rays passing through the cavitating flow. The source, Yxlon Y.TU 160-D06, was operated at 120 keV and 5 mA in order to achieve a high contrast between the cavities and the fluid. The flat detector, Xineos-3131 CMOS model, consists of a $307 \text{ mm} \times 302 \text{ mm}$ sensitive area with a 1548×660 pixel array. Each pixel has a size of $198 \mu\text{m} \times 198 \mu\text{m}$ with 14 bits of pixel depth, resulting in a spatial resolution of about 0.07 mm in the imaging plane. Images were recorded at 60 Hz over 60 s. Schematics of the measurement setup are illustrated in figure 2.

The experimental setup shown in figure 1 was reoriented for the x-ray imaging measurements due to space constraints. Nevertheless, the flows from the two experiments at the same cavitation number were confirmed to be equivalent, as the pressure drops across the venturi (Δp) were nearly identical for both cases. Visual inspection also confirmed symmetry of the top and bottom halves of the time-averaged shadowgraphs (for example, see figure 6(d)), suggesting little influence of gravity.

2.2. Calibration and quality of the imaging modalities

Calibration was performed for x-ray imaging in order to eventually compute a tomographic reconstruction of the time-averaged distribution of the void fraction, assuming axisymmetric

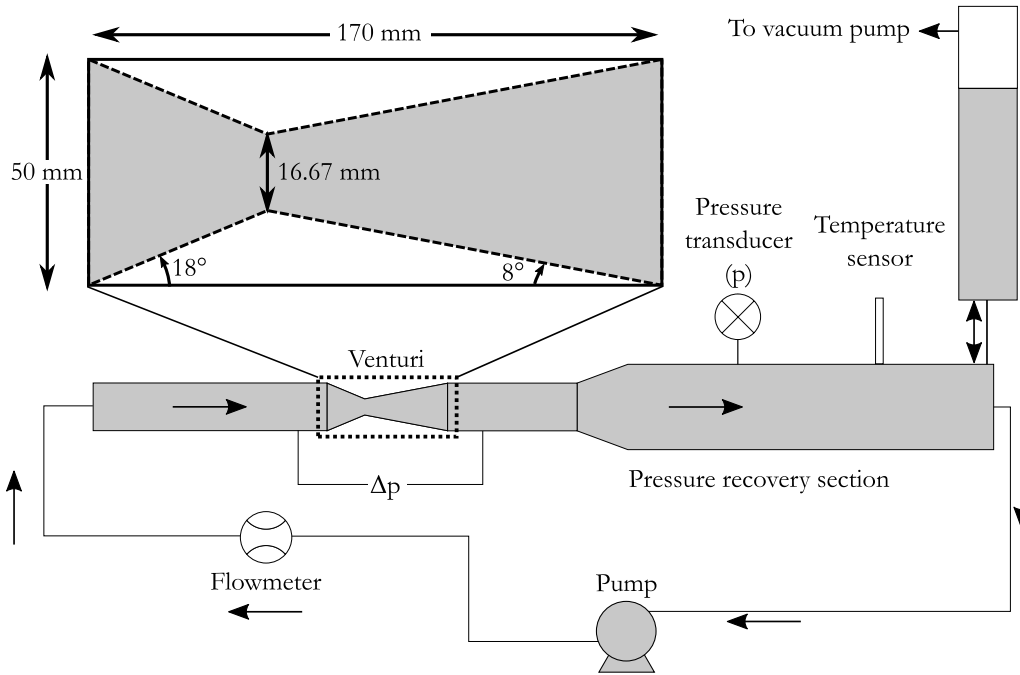


Figure 1. The flow setup deployed for the shadowgraphy measurements. Shown in the inset is a detailed version of the venturi. For the x-ray measurements, the major components of the setup were turned 90° in the counter-clockwise direction due to space limitations. Objects in this schematic are not drawn to scale.

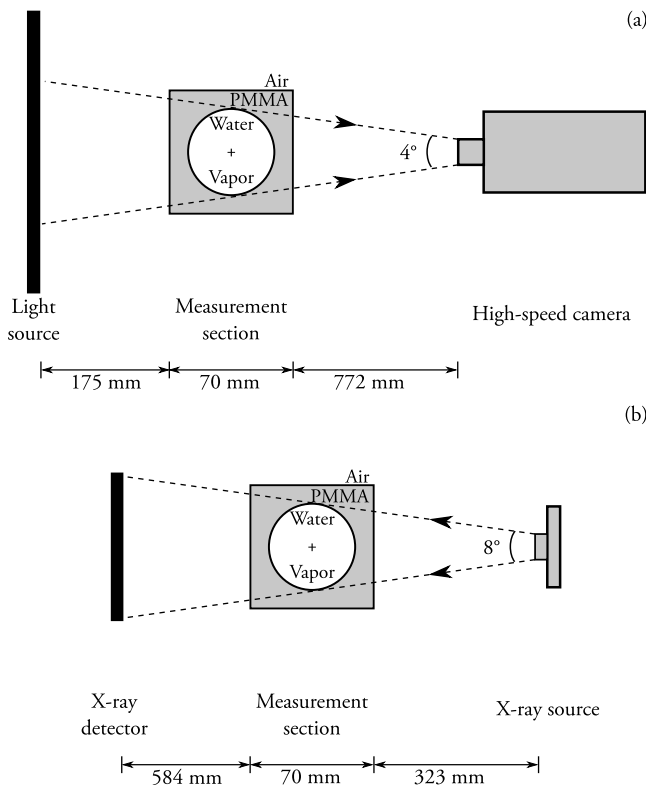


Figure 2. Imaging of the flow was done via two imaging modalities. Shown here are their respective schematics. (a) Shadowgraphy (b) x-ray imaging. Objects and viewing angles are not drawn to scale. The angles approximate the span covered by the venturi.

distribution of the two phases. As a reference, intensities were measured by the x-ray detector when the venturi contained

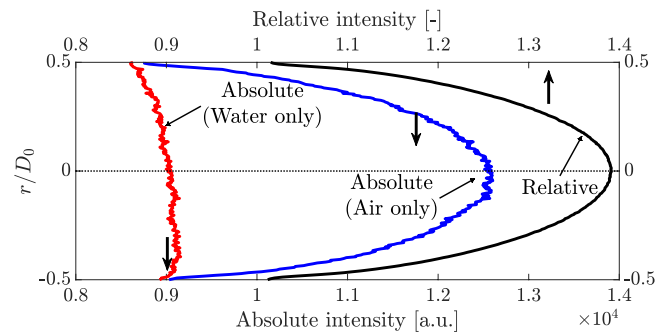


Figure 3. Profiles of the absolute and relative intensities recorded on the x-ray detectors at the streamwise location of the venturi throat. The two cases considered are when the venturi contains solely air and solely water.

only air and only water. Air is a suitable alternative for water vapor as they have similar mass densities, and thus similar linear absorption coefficients. For the calibration in air, the venturi was left empty while it was completely filled with filtered water for the latter. At the streamwise plane of the throat, the maximum intensity was recorded as 12580 for air while it was 9045 for water, as can be seen in figure 3. Thus, approximately 21% of the total capacity of the 14-bit detector was utilized here. However, this range would increase in the downstream direction with the increasing diameter of the venturi cross-section. A relative intensity profile is obtained by dividing the absolute intensities of air and water, shown in figure 3, which is in accordance with the shape of the venturi (air occupies a higher fraction of the x-ray path length closer to the center of the venturi). Moreover, the wiggles visible in the absolute intensity curves are drastically compressed in the relative intensity curves. This confirms that

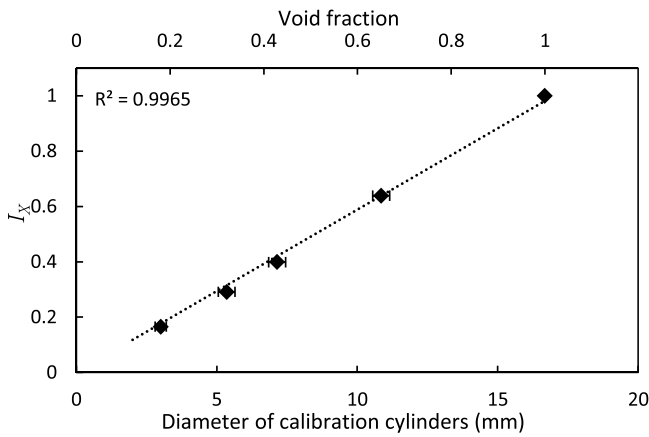


Figure 4. A linear relationship exists between the normalized x-ray image greyscale intensity (I_X) and the line-integrated void fraction, calculated by means of the plastic cylinders diameter. The intensities are measured at the centerline ($r/D_0 = 0$ in figure 3).

the wiggles in the absolute intensities are a result of the differences in individual x-ray detector element sensitivities and not random noise.

Furthermore, air-containing calibration cylinders of four different diameters and negligible thicknesses were inserted into the venturi, which was already filled with water. The calibration cylinders were aligned with the axis of symmetry of the venturi. Calibration was then performed at four different streamwise locations by recording the mean intensity along the centerline of the cylinder, averaged over 3700 frames. As the diameters of the calibration cylinders were known, the intensity at the center of the cylinder related to the line-integrated void fraction. A linear relationship was obtained between the normalized intensity in the x-ray images (I_X) and diameter of plastic cylinders (and thus, the line-integrated void fractions), as shown in figure 4. This implies that the normalized intensity can be used directly in place of the line-integrated void fraction for comparison with shadowgraphy images. Moreover, this linear correlation might also hint at the absence of beam hardening in the current experiments. Most x-ray sources emit a broad range of energies. Beam hardening is the phenomenon whereby the lower energy photons are preferentially absorbed by the matter it passes through [23]. Beam hardening would be an important issue, had the material possessed higher absorption coefficients than the materials in the current experiments [24].

The standard error of mean for the measured intensities for the various calibration cylinders was found to be less than 0.05%, which is considered acceptable. The standard deviation of the normalized intensities gives an estimate of the resolution of void fractions, which is approximately 3%. The dynamic range for these measurements is the ratio between the maximum detectable void fraction and the resolution of the void fraction measurement, which in the current study is approximately 33.

A calibration procedure was not performed for shadowgraphy to correct for image distortion induced by the PMMA-water interface. However, this is not expected to introduce a

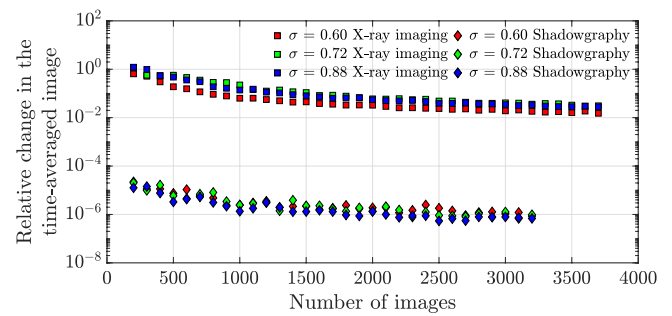


Figure 5. Sufficient convergence is obtained for the time-averaged greyscale images via x-ray imaging as well as shadowgraphy.

major error as the overall distortion error is less than one pixel [25].

3700 x-ray images were used in the calibration shown in figure 4. A similar number of images were utilized for the cavitating flow measurements. In order to ensure that the quantity of images was sufficient, a convergence study was performed on the images of the cavitating flow whose results are shown in figure 5. The term on the y-axis is computed as follows. After each 100 images, a new time-averaged image is computed, say I_{new} , is then compared with the old time-averaged image (i.e. without the new 100 images), say I_{old} . The term on the y-axis is then mean of all values in the matrix $|(I_{new} - I_{old})/I_{old}|$. It is seen that after 3700 images, the relative error reduces to less than 3%, implying sufficient convergence. A similar analysis for the shadowgraphy images is performed, which too shows a satisfactory convergence behaviour. The quicker convergence of the shadowgraphy images may be attributed to the better signal to noise ratio.

2.3. Data processing

Images acquired by the two techniques have several differences, including the aspect ratio, spatial resolution, field of view, lines-of-sight and greyscale intensities. Therefore, a few preprocessing steps were needed before comparing the two types of images. All of the following steps were performed using Matlab R2016b (The Mathworks Inc., Natick, USA). The process is illustrated in figure 6, and the bulk flow is from left to right in each of these images.

In order to reduce the effect of the system on the image analysis, a background subtraction was performed first. For the x-ray technique, images of the non-cavitating flows (i.e. vapour absent) were available. However, no such images were available for the shadowgraphy experiments. Thus, artificial background images were generated for the shadowgraphy technique as follows. Each pixel in the background image is assigned with the maximum greyscale value (in shadowgraphy, the liquid phase appeared white) measured at that pixel location over the course of the entire measurement (multiple cavitation cycles). This method also leads to the generation of a few thin artifacts (for example, near the top wall in figures 6(e) and (f)). However, these are not expected to significantly affect the results and conclusions of this study.

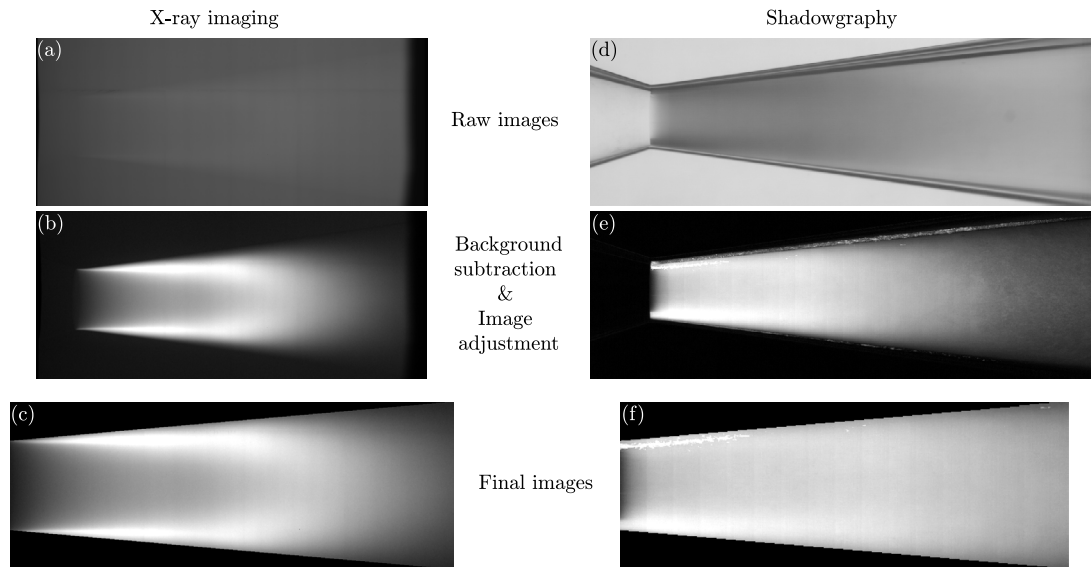


Figure 6. Images from the two measurement techniques were preprocessed in order to make them comparable. (a)–(c) correspond to images from the x-ray imaging technique while (d)–(f) are the corresponding steps for shadowgraphy images. ((a) and (d)) are the raw time-averaged images. ((b) and (e)) are the images obtained following a background subtraction as well as being adjusted to improve contrast. ((c) and (f)) are the images obtained after the region of interest is cropped out. Images (c) and (f) are then mapped onto an identical coordinate space in order to compare the greyscale intensities from the two techniques. In all these images, the bulk flow occurs from the left to the right.

In the x-ray images, the vapor phase has higher greyscale intensities while the liquid phase had lower ones. This happens because the presence of vapor leads to lower attenuation of the x-rays along its path length. On the other hand, the shadowgraphy images have lower greyscale intensities for the vapour phase and vice versa. This occurs as the bubbles generated by cavitation block the visible light emanating from the LED panel. Thus, for the x-ray images, the background is subtracted from the raw time-averaged images while for the shadowgraphy images, the raw time-averaged image is subtracted from the background. This way, the lower greyscale intensities represent the liquid phase in both sets of background-subtracted images.

While the shadowgraphs display a clear contrast between the two phases (via the greyscale intensities), the contrast is visibly reduced for the x-ray images (figure 6(a)), due to the higher background greyscale intensities. For example, in figure 3, the background greyscale has approximately 9000 counts. When the venturi is emptied, the measured intensity is approximately 12500 counts. The maximum contrast at the throat is thus approximately 40% of the background signal. However, in the actual experiments, the void fractions seldom reach close to 100%, and the recorded signals are closer to the bottom portion of the 40% range. While this range may be improved by operating the x-ray source at a higher power, it would lead to saturation of the CMOS sensor. Thus, an image adjustment operation (i.e. rescaling the greyscale intensities in order to have 1% of the values being saturated at low and high intensities) is performed on both sets of images, which effectively normalizes the greyscale intensities. With this operation, the values of the greyscale intensities then vary between 0 and 1 in both cases.

The next step involves the cropping of images to restrict the analysis to a certain region of interest. The center of

the venturi throat is selected as the origin for the current analysis with a length of five throat diameters ($5D_0$, where D_0 is the throat diameter) used in the streamwise direction. Furthermore, the diameter of the region of interest in the radial direction increased with respect to the throat diameter with a divergence angle of 5° along the downstream direction, which is lower than the venturi divergence angle of 8° . This is done so in order to avoid analysis in the upper and lower wall regions, which might be susceptible to errors via optical distortion, especially in shadowgraphy, despite a close match in refractive indices.

Since the images from the two experiments possess different resolutions, it is desirable to ultimately map the greyscale intensities from the two measurement techniques onto the same pixel coordinates. The throat diameter is used as a reference length scale to adjudge the goodness of the overlap between the coordinate systems. In the current analysis, information from the shadowgraphy images (lower spatial resolution) is interpolated onto pixel coordinates of the x-ray images (higher spatial resolution) via linear interpolation. The original disparity between the image resolutions (figures 6(a) and (b)) is dispensed with (figures 6(e) and (f)). Thus, images from the two techniques can now be compared on a pixel-by-pixel basis.

3. Results

Greyscale intensities from both techniques are rendered comparable after the processing of images per the procedure in section 2.3. The comparison here is primarily restricted only to the regions located near the line of symmetry, along the streamwise direction. This is done so in order to avoid artifacts that may arise due to the stronger curvature of the pipe away

from the line of symmetry, especially in the shadowgraphy images. Moreover, this minimizes any effects that may arise due to the minor difference in the viewing angles between the two methods.

Three different cavitation numbers are considered for comparison in the current study: 0.60, 0.72 and 0.88, whose results are illustrated in figures 7–9 respectively. This was done as each cavitation number had different vapor distributions [22]. For each case, the time-averaged greyscale intensity image from both the techniques are shown, with the regions of interest overlaid on them. It can be seen that there is a similarity in a qualitative sense (for example, the streamwise location beyond which the greyscale intensity is monotonically decreasing). However, there are much sharper structures visible in the x-ray images as compared to the shadowgraphy ones, owing to the former's ability in penetrating the multiple media. Thus, it is expected that the greyscale intensities from the two modalities will not behave in a coherent manner, quantitatively.

To this end, a quantitative comparison of the greyscale intensities from the two techniques is performed. This is done so by dividing the entire domain into smaller regions of interest or zones. Points (or pixels) from each zone can then be placed onto a coordinate space, formed by the greyscale intensities in x-ray images (I_X) and shadowgraphy images (I_S). Using these scattered points, a local correlation coefficient, C_l , can be defined for each zone. C_l quantifies the correlation between the greyscale intensities obtained by the two techniques. The division of the entire domain into zones is performed with two considerations. Firstly, these zones should be small enough to allow for a good spatial resolution of these local correlation coefficients. Secondly, these zones should be large enough to contain sufficient scatter points. Decreasing the size of the zone will lead to having fewer scatter points, which may even collapse around the same point. This might lead to an incorrect interpretation of the local correlation coefficient. Thus, the domain was divided into three zones along the radial direction and into six along the streamwise direction. The number of sampling points increases from about 15000, in the zones nearest to the throat, to 25000, in the zones furthest from the throat, due to the diverging nature of the test section.

The local correlation coefficients are then shown in figures 7–9(c), for the three cavitation numbers. In each case, it is seen that there is an initial short region with acceptable positive correlation coefficients which quickly begin to deteriorate along the downstream direction, even reaching negative values (for the higher cavitation numbers). This region is then followed by a region of recovery in the correlation coefficients back to a stable, high, positive value. However, these deterioration and recovery lengths are clearly dependent on the cavitation number.

The above behavior of the correlation coefficients can also be seen in the colour-coded scatter points shown in figures 7–9(d). The colour-coded scatter points correspond to locations in the local zones of the same colour shown in figures 7–9(a) and (b). It is seen that the scatter points in the zones follow a loop-like trajectory along the downstream direction. The

Table 1. Slopes of the approximate linear fits as well as non-dimensional cavity lengths in figures 7–9. m_n denotes the slope of the line n while the cavity length (L_c) is normalized by the throat diameter (D_0). C_g is the global correlation coefficient.

σ	m_1	m_2	m_3	$\frac{L_c}{D_0}$	C_g
0.60	3.49	0.18	0.34	3.54	0.77
0.72	2.90	−0.45	0.36	3.02	0.80
0.88	4.33	−2.05	0.55	1.82	0.81

trajectories in each of the three cases have three distinct linear regions. The first line corresponds to the aforementioned region with an acceptable positive correlation coefficient, while the second and third lines are related to the regions of deteriorating and recovering correlation coefficients, respectively. For the cavitation numbers of 0.72 and 0.88, the second line even has a negative slope.

Another quantity of interest here is the cavity length (L_c), or the streamwise length of the cavity along the venturi walls, immediately before it detaches and vortices are shed. Cavity lengths are derived using the shadowgraphy images, based on the formulation used by Long *et al* [26]. It is expressed as $L_c = D_0 \cdot (L_{c,\text{pix}}/D_{0,\text{pix}})$. Here, $L_{c,\text{pix}}$ and $D_{0,\text{pix}}$ are the cavity length and throat diameter, respectively, in number of pixels. The same procedure is not applicable to the x-ray data due to a poor signal-to-noise ratio in the instantaneous x-ray images. The cavity length for all the three cavitation numbers is located near the onset of the third ‘correlation regime’ (or Line 3).

Slopes of these three lines along with the cavity length and the global correlation coefficient (C_g , correlation coefficient obtained by considering the entire venturi) are summarized in table 1. The relatively high global correlation coefficient underlines that the two images provide a similar information qualitatively.

4. Discussion

The results demonstrate the absence of universal quantitative congruity between greyscale intensities obtained via shadowgraphy and x-ray imaging. This result is not very surprising given that shadowgraphy would not be expected to successfully tackle opaque media. These observations are also in line with the qualitative results of Mitroglou *et al* [20] and Lorenzi *et al* [21]. What distinguishes the images from the two techniques is the amount of recognizable information about the flow structures, as stated previously. In the following discussion, it is assumed that the x-ray intensities (I_X) represent the ground truth (since it strongly relates to the line-integrated void fractions, as established previously in section 2.2).

The presence of an initial positive correlation (denoted as Line 1 in figures 7–9(d)) immediately downstream of the venturi throat is common to all the cavitation numbers. This arrives from the fact that there is a gradual rise in the greyscale intensities in both sets of images. In the region furthest downstream from the throat, both sets of images are characterized by gradually decreasing greyscale intensities, which leads to the formation of a second positively correlated region

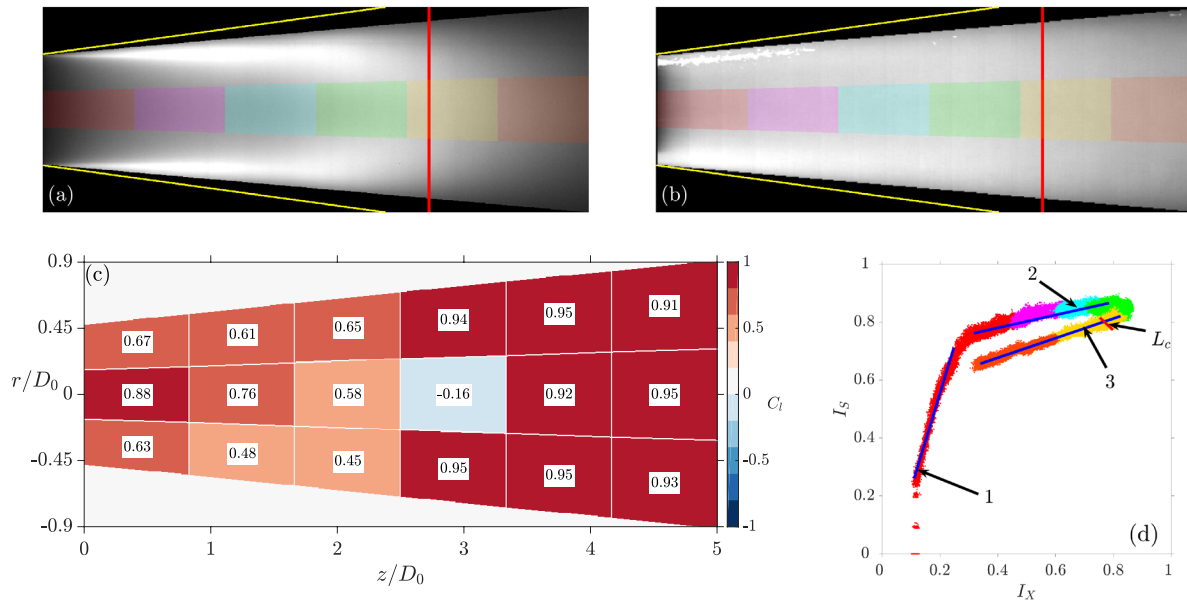


Figure 7. A comparison of the greyscale intensities at identical coordinates along the streamwise direction, from the two measurement techniques. Here, $\sigma = 0.60$. (a) Time-averaged x-ray image with the regions of interest superimposed in different colours, (b) time-averaged shadowgraphy image with the regions of interest superimposed in different colours, (c) local correlation coefficients at the different zones, (d) the colour-coded zonal scatter plots. The colours in this scatter plot correspond with the respective coloured regions of interest demarcated in (a) and (b). The vertical red lines in (a) and (b) denote the streamwise location of the estimated cavity length. The red line in (d) is the approximate location of the estimated cavity length along the loop-like trajectory in the scatter plot, while the blue lines in (d), labeled from 1–3, identify the different regimes. In (a) and (b), darker regions represent the liquid phase while the lighter regions represent the vapor phase. The yellow lines in (a) and (b) denote the venturi walls.

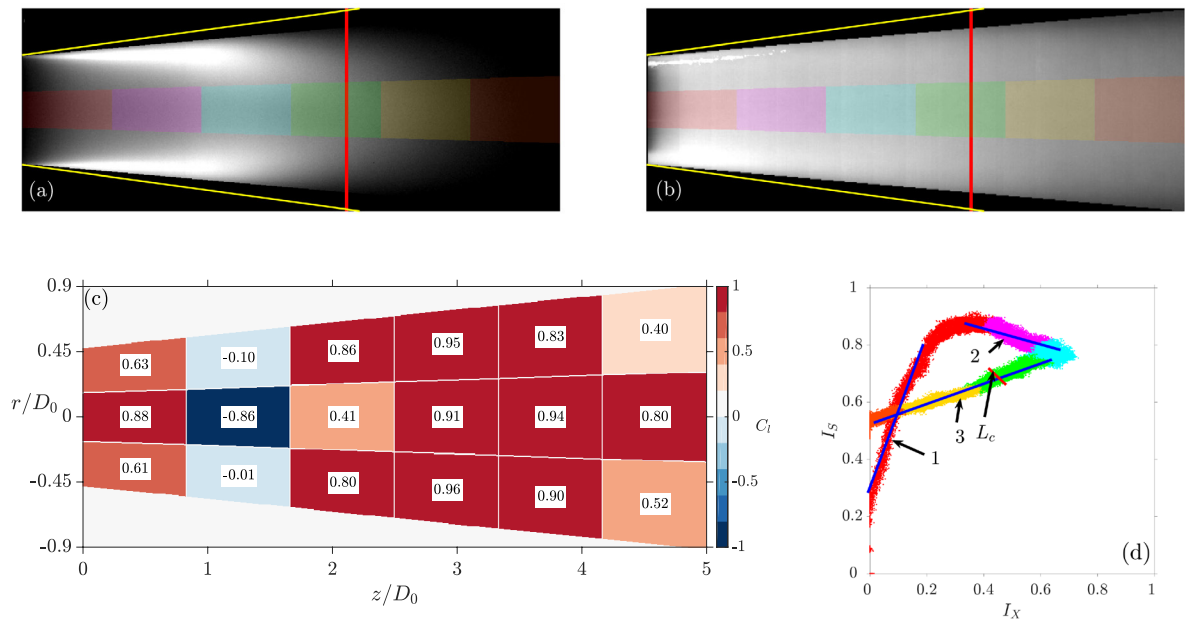


Figure 8. A comparison similar to that shown in figure 7 was also performed for $\sigma = 0.72$. See caption of figure 7 for more details.

(denoted as Line 3 in figure 7–9(d)). As shown in table 1, the slopes of these two regions (Line 1 and Line 3) are not equal. The region in between the aforementioned two regions (denoted as Line 2 in figures 7–9(d)) displays contrasting correlation behaviour. The central regions of the x-ray images, like the shadowgraphy ones, are characterized by an initial rise in greyscale intensities followed by a region of continuous decline. However, the streamwise length over which this

increase happens is considerably larger for the x-ray images than in the shadowgraphy images (at least for σ of 0.72 and 0.88), which leads to a region of negative correlations in these two cases.

A hypothesis for the above observations is postulated, and illustrated through a simplified schematic in figure 10. Three regimes have been demarcated. The initial region immediately downstream of the throat is occupied by a swarm of

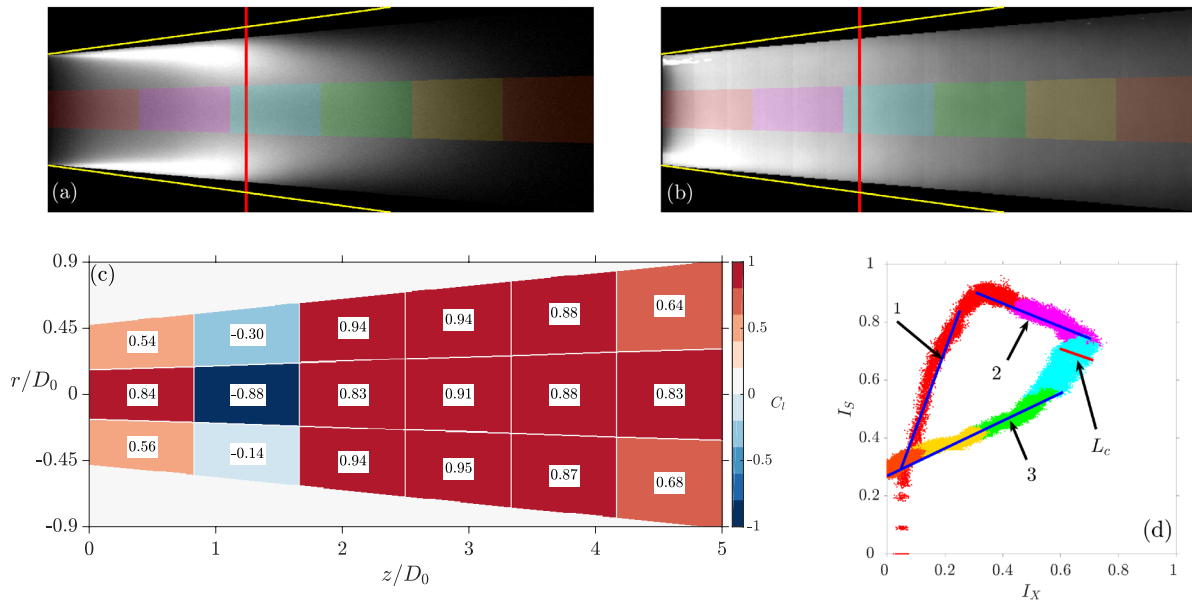


Figure 9. A comparison similar to that shown in figure 7 was also performed for $\sigma = 0.88$. See caption of figure 7 for more details.

tiny bubbles, forming streaks. In this region, the density of the bubbles is low enough for shadowgraphy to return a reliable impression of the void fractions. Since visible light still has good penetrability, a modified Beer–Lambert law [27] for the transmittance of light may still be applicable. The second region is characterized by the bubbles having coalesced into a thicker film which exists very close to the venturi walls. This is a problem for the shadowgraphy technique, as the camera is unable to capture information from any depth beyond the cavities near the wall. The cavity basically acts as a specular reflector for light. The third region, usually downstream from the cavity length location, is characterized by detached cavities that have drifted away from the wall, and towards the center, followed by a collapse of the cavitation cloud into smaller bubbles. Further downstream, a fully liquid phase is recovered.

The presence of distinct regimes can be confirmed via the tomographic reconstruction of the vapor content at multiple cross-sections, illustrated in figure 11. This tomographic reconstruction has been done via the x-ray images. Filtered back projection is applied to the cone-beam 2D time-averaged x-ray image using the ASTRA Toolbox [28]. A detailed explanation of this reconstruction is available in Jahangir *et al* [29]. One disadvantage of these time-averaged reconstructions is its inability to distinguish a coalesced cavity film from a swarm of tiny bubbles, occupying the same volume.

Four cross-sections have been considered here. It is clear that there is a development of a cavity film-like structure near the circumference of the cavity, whose thickness increases in the streamwise direction (for example, consider Sections A and B in figure 11). When sufficiently thick, this film would be obstructive for the shadowgraphy technique. This would correspond to regime 2 hypothesized in figure 10. However, beyond a certain point, these cavities drift away from the walls and begin to collapse (for example, consider Sections C and D in figure 11). This cavity detachment and subsequent

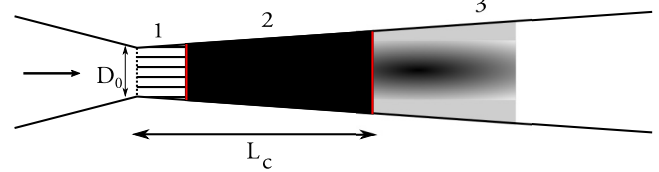


Figure 10. Three different regimes are observed in the shadowgraphy images pertaining to the current geometry. In this schematic, the darker the shade, the higher the vapor phase visualized. Regime 1: streaks of tiny vapor bubbles. Regime 2: cavity grows in size near the venturi walls, acting as a specular reflector to visible light. Regime 3: cavity moves away from the walls, and collapses. The flow is from left to right.

regeneration of the liquid phase would be beneficial for shadowgraphy. This would correspond to regime 3 illustrated in figure 10.

On first sight, it appears that regime 1 shown in figure 10 is absent in the tomographic reconstructions considered in figure 11. This happens due to the smoothing of the bubble streaks in the time-averaged images. Thus, an instantaneous snapshot from the shadowgraphy measurements is considered in figure 12, which too illustrates the different regimes. Regime 1, in the short distance immediately downstream of the throat, has short streaks of tiny bubbles along the walls, which does not hinder the camera’s view much. This explains the initial region of positive correlation from the intensity comparison graphs (figures 7–9(d)). By the time the bubbles coalesce near the walls to form a cavity film, the vapor fraction near the walls is high enough to obstruct the camera’s view and give an incorrect impression of the void fraction. This returns the region with relatively poorer correlation coefficients from the intensity comparison graphs. Downstream of the streamwise location of the cavity length, the cavity detaches from the circumferential wall, meanders towards the center, before collapsing into tinier bubbles and turning back into the liquid phase. This region marks an improvement in the correlation

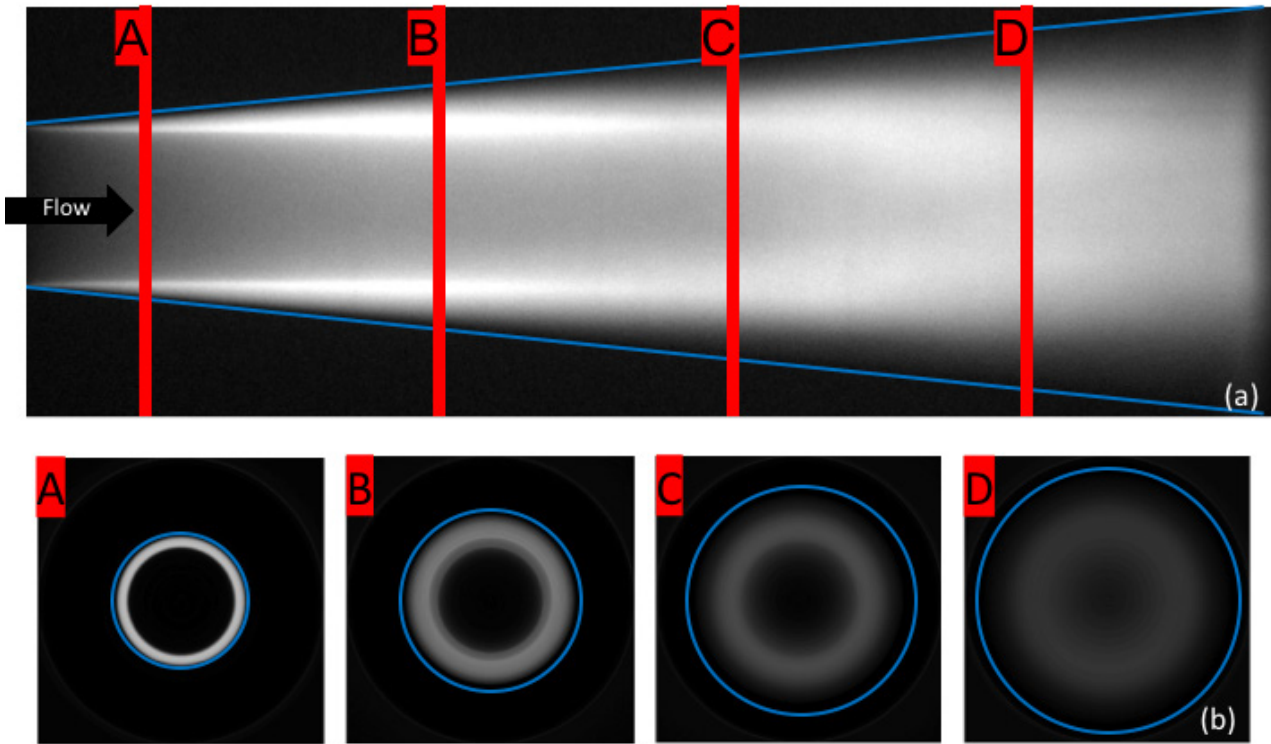


Figure 11. Tomographic reconstruction of the void fractions. Sections A and B illustrate the presence and development of a cavity film near the wall circumference while Sections C and D exemplify the detachment, drifting towards the centerline and subsequent collapse of the cavity film. (a) The streamwise locations of the four different planes considered. The venturi walls are shown in blue. (b) Tomographic reconstruction of the void fractions in the above four cross-sections. Lighter greyscale values indicate higher presence of vapor and vice versa. Here, $\sigma = 0.47$.

coefficients comparing the two techniques. Upon taking a time average of many such instantaneous images, a smoother version of the instantaneous snapshot in figure 12 shall be obtained. The intermittency of the flow would also determine the greyscale intensities in the time-averaged image.

It should also be noted that a correlation coefficient close to unity simply implies the existence linear relation between the quantities being compared (i.e. $I_S = m \cdot I_X$, where m is arbitrary). If actual line-integrated void fractions were being compared instead of intensities, the slope relating the line-integrated void fractions extracted from the two techniques would have to equal unity in order to establish equivalency of the two imaging techniques. However, such a comparison is not possible as the greyscale intensities from shadowgraphy do not have a straightforward relation with line-integrated void fractions. For example, in both cases, where the venturi contains only air or only water, identical greyscale intensities would be recorded by shadowgraphy. For this reason, an uncertainty analysis on the accuracy of shadowgraphy for void fraction estimation is impractical.

In quantifying void fractions from x-ray imaging, the two dimensional x-ray image possessing information on the line-integrated void fractions, is only an intermediate step. A tomographic reconstruction akin to the one shown in figure 11 would be necessary for local void fraction quantification. A hypothetical tomographic reconstruction of the 2D

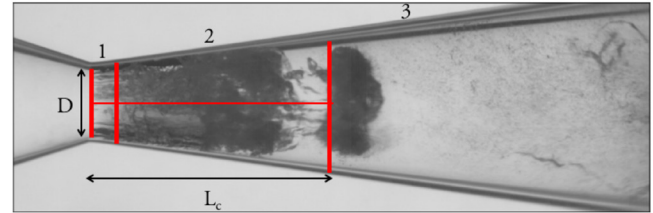


Figure 12. An instantaneous snapshot from the shadowgraphy experiment for $\sigma = 0.60$, supporting the presence of the three regimes proposed in figure 10. Regime 1: thin streaks of tiny bubbles along the circumference. Regime 2: the cavitation film develops near the walls of the venturi. Regime 3: the cavity drifts away from the walls while moving towards the center, and in the subsequent snapshots, it collapses into tinier bubbles with the liquid phase being regenerated further downstream. The vertical red lines demarcate the three regimes.

shadowgraphy images would give different estimates of the void fraction than that of x-ray, stemming from the differences in the original 2D images. Thus, it can be said that quantitative estimates of the void fraction in cavitating flows from time-averaged shadowgraphy experiments are likelier to represent the truth, only in regions with low fractions of dispersed bubbles or detachment of the cavities from the walls (regimes 1 and 3). However, it is highly likely to provide improper estimates of the void fractions in regions with coalesced cavities near the walls, as evidenced by the regions of negative

correlations for cavitation numbers of 0.72 and 0.88. These conclusions could also be extrapolated to the other multiphase flows introduced at the beginning of this article.

An influential factor that has been unaccounted for in the entire analysis thus far, is the relative placement of the measurement section (venturi) with respect to the illuminating source (LED panel/x-ray source) and detector (high-speed camera/x-ray detector). It can be expected that a configuration different to the one used in the current study would result in a different greyscale intensity map in the 2D images. This would be a result of a new line of sight between the source and the detector. Eventually, this would translate into a different estimate of the void fraction at a given location. However, this factor is not expected to affect the qualitative hypothesis postulated in figure 10, i.e. on the applicability of shadowgraphy to the three regimes. Nevertheless, differences can be expected in the cavity lengths as well as the slopes of the linear fits to local correlation coefficients in table 1.

A look-up table like procedure to correlate the void fractions and the greyscale intensities in shadowgraphy images can be implemented for the different regions. This would allow for a more accurate estimation of void fractions via shadowgraphy, especially when knowledge of the precise locations of the regimes is available. However, if this information is unavailable, the look-up table would prove fruitless, as there is no unique value of line-integrated void fraction for a single greyscale intensity obtained by shadowgraphy. For example, $I_S = 0.4$ in figure 9(d) has two possible values for I_X , depending on the regime under consideration. Constructing and implementing a careful look-up table procedure for different regimes in an internal flow is likely to prove an arduous task.

5. Conclusions

Images from shadowgraphy and x-ray measurements were compared. Correlations were made based on the greyscale intensity values along the streamwise direction for a cavitating flow through a venturi, at three different cavitation numbers of 0.60, 0.72 and 0.88. It was assumed that the information obtained through the x-ray imaging technique represented the truth.

Three distinct ‘correlation regimes’ were identified for the flow considered. The first region, associated with a swarm of tiny bubbles along the walls, is short in extent with a positive correlation between the greyscale intensity values from the two techniques. The second region, associated with a cavity film growing near the wall, shows more variability across the different cavitation numbers and may display either a positive ($\sigma = 0.60$) or a negative ($\sigma = 0.72$ and 0.88) correlation. The third region, associated with the drifting of the cavity away from the walls towards the central region of the venturi as well as collapse of the cavities, is found beyond the estimated location of the cavity lengths. While shadowgraphy may still return reliable estimates of void fractions in flows resembling the first and third regions, it could lead to

improper conclusions about the void fraction profiles in flows that resemble the second region.

Acknowledgments

AD and SJ contributed equally to this paper. CP and AD have received funding from ERC Consolidator Grant 725183 ‘OpaqueFlows’. SJ has received funding from the European Union Horizon 2020 Research and Innovation programme, Grant Agreement No 642536. The authors would like to thank Rob Mudde and Evert Wagner (Transport Phenomena, TU Delft) for facilitating the x-ray measurements. The authors further thank Willian Hogendoorn (Multiphase Systems, TU Delft) for providing access to the high-speed shadowgraphy data.

ORCID iDs

Amitosh Dash  <https://orcid.org/0000-0001-6109-0562>
 Saad Jahangir  <https://orcid.org/0000-0002-3520-5722>
 Christian Poelma  <https://orcid.org/0000-0001-8676-9221>

References

- [1] Van Ommen J R and Mudde R F 2008 Measuring the gas–solids distribution in fluidized beds—a review *Int. J. Chem. React. Eng.* **6** R3
- [2] Nadeem H and Heindel T J 2018 Review of noninvasive methods to characterize granular mixing *Powder Technol.* **332** 331–50
- [3] Khlifa I, Vabre A, Hočevcar M, Fezzaa K, Fuzier S, Roussette O and Coutier-Delgosha O 2017 Fast x-ray imaging of cavitating flows *Exp. Fluids* **58** 157
- [4] Wang D, Song K, Fu Y and Liu Y 2018 Integration of conductivity probe with optical and x-ray imaging systems for local air–water two-phase flow measurement *Meas. Sci. Technol.* **29** 105301
- [5] Gnanaskandan A and Mahesh K 2016 Large Eddy Simulation of the transition from sheet to cloud cavitation over a wedge *Int. J. Multiph. Flow* **83** 86–102
- [6] Ganesh H, Mäkiharju S A and Ceccio S L 2016 Bubbly shock propagation as a mechanism for sheet-to-cloud transition of partial cavities *J. Fluid Mech.* **802** 37–78
- [7] Ursenbacher T, Wojtan L and Thome J R 2004 Interfacial measurements in stratified types of flow. Part I: new optical measurement technique and dry angle measurements *Int. J. Multiph. Flow* **30** 107–24
- [8] Wojtan L, Ursenbacher T and Thome J R 2004 Interfacial measurements in stratified types of flow. Part II: measurements for R-22 and R-410A *Int. J. Multiph. Flow* **30** 125–37
- [9] Wojtan L, Ursenbacher T and Thome J R 2005 Measurement of dynamic void fractions in stratified types of flow *Exp. Therm. Fluid Sci.* **29** 383–92
- [10] Dunn P F, Thomas F O, Davis M P and Dorofeeva I E 2010 Experimental characterization of aviation-fuel cavitation *Phys. Fluids* **22** 117102
- [11] Leandro J, Carvalho R, Chachereau Y and Chanson H 2012 Estimating void fraction in a hydraulic jump by measurements of pixel intensity *Exp. Fluids* **52** 1307–18
- [12] Puli U and Rajvanshi A 2012 An image analysis technique for determination of void fraction in subcooled flow boiling of

- water in horizontal annulus at high pressures *Int. J. Heat Fluid Flow* **38** 180–9
- [13] Wosnik M and Arndt R E 2013 Measurements in high void-fraction bubbly wakes created by ventilated supercavitation *J. Fluids Eng.* **135** 011304
- [14] Rana K, Agrawal G, Mathur J and Puli U 2014 Measurement of void fraction in flow boiling of ZnO–water nanofluids using image processing technique *Nucl. Eng. Des.* **270** 217–26
- [15] Leandro J, Bung D and Carvalho R 2014 Measuring void fraction and velocity fields of a stepped spillway for skimming flow using non-intrusive methods *Exp. Fluids* **55** 1732
- [16] Perpar M, Polutnik E, Pečar M and Žun I 2014 Bubbly structures in a cavitating slot orifice *Exp. Therm. Fluid Sci.* **53** 57–69
- [17] Kowalski K, Pollak S, Skoda R and Hussong J 2018 Experimental study on cavitation-induced air release in orifice flows *J. Fluids Eng.* **140** 061201
- [18] Wang C, Huang B, Zhang M, Wang G, Wu Q and Kong D 2018 Effects of air injection on the characteristics of unsteady sheet/cloud cavitation shedding in the convergent-divergent channel *Int. J. Multiph. Flow* **106** 1–20
- [19] Bauer D, Chaves H and Arcoumanis C 2012 Measurements of void fraction distribution in cavitating pipe flow using x-ray CT *Meas. Sci. Technol.* **23** 055302
- [20] Mitroglou N, Lorenzi M, Santini M and Gavaises M 2016 Application of x-ray micro-computed tomography on high-speed cavitating diesel fuel flows *Exp. Fluids* **57** 175
- [21] Lorenzi M, Mitroglou N, Santini M and Gavaises M 2017 Novel experimental technique for 3D investigation of high-speed cavitating diesel fuel flows by x-ray micro computed tomography *Rev. Sci. Instrum.* **88** 033706
- [22] Jahangir S, Hogendoorn W and Poelma C 2018 Dynamics of partial cavitation in an axisymmetric converging-diverging nozzle *Int. J. Multiph. Flow* **106** 34–45
- [23] Bushberg J T and Boone J M 2011 *The Essential Physics of Medical Imaging* (Baltimore, MD: Williams & Wilkins)
- [24] Mudde R F 2010 Time-resolved x-ray tomography of a fluidized bed *Powder Technol.* **199** 55–9
- [25] Hogendoorn W 2017 Cavitation: experimental investigation of cavitation regimes in a converging-diverging nozzle *Master's Thesis* Delft University of Technology Available online at <https://repository.tudelft.nl/islandora/object/uuid:823a18f0-66a8-4ffd-a688-c3dadf62c4da?collection=education>
- [26] Long X, Zhang J, Wang J, Xu M, Lyu Q and Ji B 2017 Experimental investigation of the global cavitation dynamic behavior in a venturi tube with special emphasis on the cavity length variation *Int. J. Multiph. Flow* **89** 290–8
- [27] Wind L and Szymanski W 2002 Quantification of scattering corrections to the Beer-Lambert law for transmittance measurements in turbid media *Meas. Sci. Technol.* **13** 270
- [28] Van Aarle W, Palenstijn W J, Cant J, Janssens E, Bleichrodt F, Dabravolski A, De Beenhouwer J, Batenburg K J and Sijbers J 2016 Fast and flexible x-ray tomography using the ASTRA toolbox *Opt. Express* **24** 25129–47
- [29] Jahangir S, Wagner E C, Mudde R F and Poelma C 2018 X-ray computed tomography of cavitating flow in a converging-diverging nozzle *Proc. of the 10th Symposium on Cavitation (CAV2018)* (ASME)